Research Article Vol. 57, No. 29 / 10 October 2018 / Applied Optics 8757

applied optics

Method to improve the resolution of a non-parallel Fabry–Perot etalon

Xusheng Xia,[1,2] Hong Yuan,[1,2] Jinbo Liu,[1] Baodong Gai,[1] Xianglong Cai,[1] Jingwei Guo,[1,*] Yuqi Jin,[1] and Fengting Sang[1]

[1]Key Laboratory of Chemical Lasers, Dalian Institute of Chemical Physics, Chinese Academy of Sciences, Dalian 116023, China
[2]University of Chinese Academy of Sciences, Beijing 100049, China
*Corresponding author: jingweiguo@dicp.ac.cn

Received 6 August 2018; accepted 12 September 2018; posted 17 September 2018 (Doc. ID 341285); published 10 October 2018

A new method to improve the resolution of a slightly non-parallel solid etalon is proposed. The method is aimed to reduce the spectrum broadening caused by non-parallel surfaces; it contains a theoretical formula for adjusting image distances, and an algorithm for processing the corresponding fringe patterns. Theoretical consideration, computer simulation, experimental results, and application demonstration are given. The fringe patterns captured by a CCD showed good agreement with the computer simulation, and the resolution of a $\lambda/10$-wavefront-error etalon was improved from 3.1 GHz to 0.51 GHz. In comparison with other methods, this new method is convenient and economical.

OCIS codes: (120.0120) Instrumentation, measurement, and metrology; (140.0140) Lasers and laser optics; (010.0010) Atmospheric and oceanic optics.

https://doi.org/10.1364/AO.57.008757

1. INTRODUCTION

A Fabry–Perot (F-P) etalon is an optical component made of a transparent plate covered by two highly reflecting films. Due to the ability to obtain a high-resolution spectrum, F-P etalons have been used widely in laser technology, atmosphere optics, and ocean optics [1–3]. For those applications, improving the instrument resolution is an important topic. For example, Brillouin lidar systems have been developed to sense the acoustic speed, temperature, and viscosity of gas and liquid in recent years, and using an F-P etalon with an intensified charge-coupled device (ICCD) is a main choice to measure the extremely small Brillouin frequency shift and linewidth [4–8]. In a Brillouin lidar system, the resolution of spectra has a large effect on the calculation of frequency shifts and linewidths, so it directly determines the precision of measurement [9,10].

The resolution of an etalon has been studied for decades. The parameters to characterize the resolution of an etalon are linewidth $\Delta\nu$ and finesse F, which can be defined as the full width at half-maximum (FWHM) of the spectrum of a single-frequency laser, and free spectrum range divided by the linewidth, respectively [11]. According to the famous Rayleigh criterion, the resolution of an etalon is limited to its linewidth $\Delta\nu$; hence, the theoretical resolution of an etalon can be calculated by the interference theory. However, in practice, the finesse is usually much smaller than the theoretical value, due to the spectrum broadening caused by the surface defects [12–14]. Among those defects, non-parallelism (or misalignment for F-P interferometers) can cause a more serious problem of finesse degradation, than other surface (roughness and curvature) problems [15,16]. Moreover, non-parallelism also causes peak position shift for a single-point source and peak splitting for a multi-point source [17].

Although the mechanism of the spectrum broadening of a non-parallel etalon was studied over decades ago, little attention has been paid to solving this problem. Therefore, the aim of this research was to develop a method that can reduce the fringe broadening and improve the resolution. In this work, a new method that can reduce the spectrum broadening without losing much illuminance is developed, and it will be helpful for Brillouin lidar applications.

2. THEORETICAL CONSIDERATIONS

A. Qualitative Analysis

Before the theoretical calculating, it is necessary to analyze different causes for the etalon fringe broadening, so that we can focus on the non-parallelism and neglect other less important causes. In the traditional theory [11], an F-P etalon is considered as two strictly parallel surfaces with high reflectivity. In that case, laser transmitting through the etalon will form a series of concentric rings on the focal plane, and the intensity distribution function is

$$I = \frac{I_0}{1 + \frac{4R\sin^2(\delta/2)}{(1-R)^2}}, \tag{1}$$

$$\delta = 4\pi nh\cos\theta/\lambda, \tag{2}$$

where R is the reflectivity of the coating on the etalon, δ is the phase difference of two adjacent rays, h is the etalon thickness, n is the etalon refractive index, θ is the internal reflective angle, and λ is the wavelength. In this function, I reaches its maximum when $\delta = 2k\pi$, and the FWHM is $2(1-R)/\sqrt{R}$. If the etalon surfaces are not perfectly parallel planes as traditional theory describes, fringes on the focal plane should broaden. Thus the broadening of the fringe can be considered as the convolution of three different parts: (a) broadening caused by the non-monochromaticity of the laser; (b) broadening caused by the transmission function Eq. (1), since R cannot reach 100%; (c) broadening caused by the etalon surface defects, including the non-parallelism. The present paper focuses on non-parallelism, and the other parts of broadening would be dropped, so, in the following part three hypotheses were applied: (a) light transmitting into the etalon is single-frequency; (b) light transmitting out of the etalon exists if and only if the phase difference is equal to integral multiple of 2π; (c) etalons have no other defects except non-parallelism. These hypotheses will be checked after experiments. Using the three hypotheses, a qualitative image of a non-parallel etalon can be obtained.

Figure 1(a) shows the optical path of an ideal etalon and one of its fringes in the xz plane, where θ is the internal reflective angle and θ' is the angle of refraction in the air. In the xz plane, rays transmitting out of the etalon can be divided into two groups of parallel rays, and each group of rays focuses at a single point on the focal plane. As comparison, the two groups of output rays of a non-parallel etalon will not be strictly parallel, since the etalon thickness h is not a constant. As Eq. (2) shows, to keep $\delta = 2k\pi$ constant, θ will increase as the growing of h:

$$\theta \propto \arccos(1/h), \tag{3}$$

in which θ means the inner reflective angle of the kth order of the fringe pattern. Figure 1(b) shows the optical path of a non-parallel etalon, the thickness of which decreases in the x direction. As Fig. 1(b) shows, the blue group of rays diverge while the red group of rays converge, so, the blue and red rays will focus behind the focal plane and in front of the focal plane, respectively.

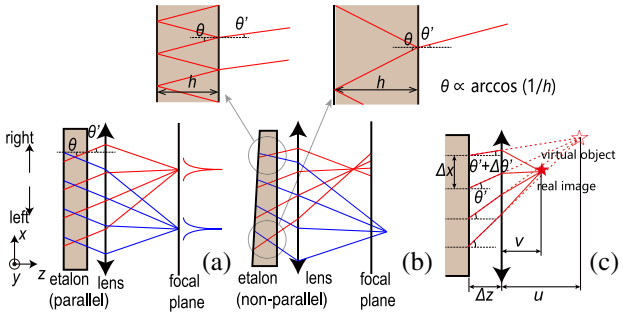

Fig. 1. (a) Optical path of a strictly parallel etalon. (b) Optical path of a non-parallel etalon. (c) Calculation of image distance v. The initiating rays are monochromatic and come from all angles (from a Lambertian radiator). The red and blue rays respectively converge on the highest and lowest points of the same order of the fringe ring. The blue group of rays in (c) was hidden for clarity.

This qualitative analysis shows the mechanism of fringe broadening in the xz plane and reveals a probable way to solve it—setting the image distance slightly longer or shorter than the focus length. This also seems like a first-order aberration that could be perfectly eliminated by tilting the CCD plane. However, this analysis only works in the xz plane, which contains the wedge angle of the etalon. Rays in the other planes cannot be simply defined as "divergent" or "convergent." Therefore, it is not a one-dimensional image error that could be perfectly solved.

B. Simplified Theory to Calculate the Image Distance

As mentioned above, rays from a non-parallel etalon will focus behind the focal plane and in front of the focal plane. A quantitative equation to calculate that image distance will be derived in this subsection.

Using paraxial approximation $\sin\theta \approx \theta$ and Snell's law $n\sin\theta = \sin\theta'$ and Eq. (2), θ' can be expressed as a function of h:

$$\theta' \approx \sin\theta' = n\sin\theta = n\sqrt{1-\cos^2\theta} = n\sqrt{1-\left(\frac{\delta\lambda}{4\pi nh}\right)^2}. \tag{4}$$

Considering that h can be expressed as $h_0 + \Delta h$ for a non-parallel etalon, and $\delta = 2k\pi$, the expression of θ' will be

$$\theta' = \sqrt{n^2 - \frac{k^2\lambda^2}{4(\Delta h + h_0)^2}} \approx \sqrt{n^2 - \frac{k^2\lambda^2}{4h_0^2}} + \frac{k^2\lambda^2}{4h_0^3\sqrt{n^2 - \frac{k^2\lambda^2}{4h_0^2}}}\Delta h.$$

Thus,

$$\frac{d\theta'}{dx} = \frac{d\theta'}{dh}\cdot\frac{dh}{dx} = \frac{k^2\lambda^2}{4h_0^3\sqrt{n^2 - \frac{k^2\lambda^2}{4h_0^2}}}\cdot\frac{dh}{dx}, \tag{5}$$

where dh/dx is the slope of the thickness as a linear function of x. The parameter dh/dx can be also interpreted as the wedge angle of etalon surfaces (in radians), so it characterizes the non-parallelism of the etalon surfaces.

On the other hand, as Fig. 1(c) shows, the object distance u has a relationship with $\Delta\theta'$ and Δx:

$$\begin{aligned}(u+\Delta z)(\tan(\theta'+\Delta\theta') - \tan\theta') &= \Delta x \\ \overset{\theta'\sim 0}{\Longrightarrow}(u+\Delta z)\Delta\theta' &= \Delta x \\ \overset{u\gg\Delta z}{\Longrightarrow} u &= \Delta x/\Delta\theta' = dx/d\theta'.\end{aligned} \tag{6}$$

Using Eqs. (5) and (6), the expression of image distance v can be obtained as

$$v = (f^{-1} - u^{-1})^{-1} = f(1 - f(\mathrm{d}\theta'/\mathrm{d}x))^{-1}$$
$$= f\left(1 - f \cdot \frac{\mathrm{d}h}{\mathrm{d}x} \cdot \frac{k^2\lambda^2}{4h_0^3\sqrt{n^2 - \frac{k^2\lambda^2}{4h_0^2}}}\right)^{-1}. \quad (7)$$

As shown in Fig. 1(b), there are two focus points, and the formula above only contains the red one. The image distance of the blue one can be easily obtained by replacing $\mathrm{d}h/\mathrm{d}x$ with $-\mathrm{d}h/\mathrm{d}x$. So the complete expression will be

$$v = f\left(1 \pm f \cdot \frac{\mathrm{d}h}{\mathrm{d}x} \cdot \frac{k^2\lambda^2}{4h_0^3\sqrt{n^2 - \frac{k^2\lambda^2}{4h_0^2}}}\right)^{-1}. \quad (8)$$

This equation shows that the adjusted image distance v is related with k; therefore, only one fringe can be accurately focused on the image plane. The fringes adjacent to the kth order fringe may also be narrowed to some degree, but not as much as the kth order.

C. Simulation

To close the gap between theories and experiments, a computer model is needed to simulate the CCD images. This model should be able to simulate the fringe patterns of a non-parallel etalon at different image distances.

It is relatively difficult to do ray tracing in this situation, as the number of rays is too large. Since rays emitted from each point of etalon distribute in a wide solid angle and the CCD resolution is 1600 × 1200 px (see Section 3), at least 1600 × 1200 rays should be calculated for each sample point of the etalon. If the etalon was divided into 100 sample points, the whole number of rays should be $1600 \times 1200 \times 100 = 1.92 \times 10^8$, which will be too large to compute. Therefore, another way was chosen to do this computer simulation.

To simplify the model, the camera lens, aperture, and etalon are put so close that the distances between them could be neglected in comparison with the lens focal length. Therefore, the distance between the etalon and the focal plane is approximately the focal length f, and the distance between the etalon and image plane is approximately the object distance v. Suppose that there is an arbitrary point $A(x, y)$ on the etalon and inside the aperture, and rays from $A(x, y)$ are focused on the focal plane. The radius of the fringe could be easily calculated by

$$r' = (\theta' f/\text{pixel size}). \quad (9)$$

The fringe was drawn as a blue circle $\odot A'$ on the focal plane [see Fig. 2(a)]. If the image plane is not the focal plane, usually the image will be blurred and be difficult to calculate. To calculate the pattern on the image plane, it could be supposed that point A is an "absolute point" (area = 0), thus the fringe will be an "absolute ring" $\odot A''$ (border width = 0). Obviously, $\odot A''$ is the projection of $\odot A'$ from point A, so the center and the radius of $\odot A''$ are $(x'', y'') = -\frac{v-f}{f}(x, y)$ and $r'' = \frac{vr}{f}$, respectively. In the same way we can draw the fringe of another point B on the etalon. It should be noticed that the radius of $\odot A'$ and $\odot B'$ may have a small difference, because the etalon thickness h is not constant. In this simulation, the thickness h decreases in the x direction; thus, h, θ, θ', and r' at B point will be larger than at A point [see Eqs. (3) and (9)].

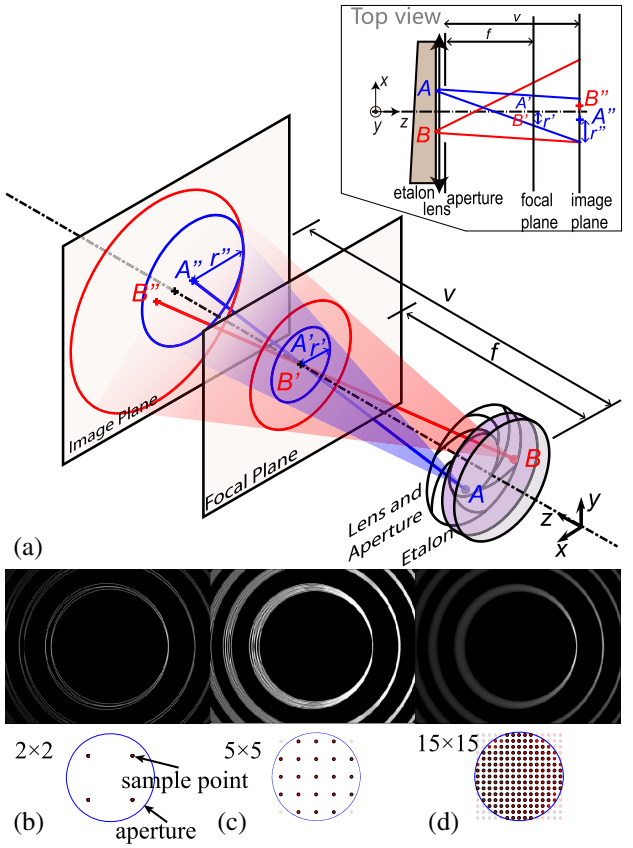

Fig. 2. (a) Schematic diagram of the computer model. The blue and red circles are fringes generated from points A and B on the etalon, respectively. The blue and red crosses mark the centers of corresponding circles, and the black crosses mark the intersection of planes and the optical axis. Note that the blue circle, the red circle, and the optical axis are concentric on the focal plane. (b)–(d) Simulations of a non-parallel etalon with 2 × 2, 3 × 3, and 15 × 15 sample points, respectively. The upper images show simulation results, and the lower plots show the location of the sample points arrays. The sample points out of the aperture were neglected in the simulation. The brightness of the simulation results was adjusted for a clear view.

As more points on the etalon were considered, the image plane would include more circles [see Figs. 2(b) and 2(c)] and would be more detailed and accurate. Among an $N \times N$ sample point array, the points in the ith column and the jth row were set at (x, y) calculated by

$$x = (2i - N - 1)/N \times r_a, \quad (10)$$

$$y = (2j - N - 1)/N \times r_a, \quad (11)$$

in which r_a is the radius of the aperture. Points out of the aperture contour should be neglected during the simulation [see Fig. 2(d) sample points array]. When N is large enough, the simulation result would seem like a continuous ring pattern with one side focused.

In this simulation, sample points were treated as "absolute points." Therefore, the fringe pattern from one single point would be an "absolute ring" (border width = 0). Actually, to create the final simulation image, the border width should have

some value. In this simulation, the border line was chosen to be a Gaussian function (border width = 3 px): Intensity = $\exp(-i^2)$, $i = -1, 0, 1$, in which i is the pixels array subscript.

Since the thickness h of each sample point can be set individually, this computer model can be used to simulate an etalon with higher-order surface defects, not only non-parallelism. This will be helpful in future studies.

3. EXPERIMENTS

A. Experimental Configuration

The theoretical results were tested using a seed-injected laser (Spectra-Physics Quanta-Ray Pro 290), a solid etalon (CVI ET-25.4-4.00-UV), and a CCD camera (PointGrey GRAS-20S4M-C, 1/1.8″). As shown in Fig. 3, the laser pulse was reflected to three diffusers which are made by fused silica, and the diffused laser then transmitted into the solid etalon, and was finally captured by a CCD camera. The CCD pixel size is 4.4 × 4.4 μm and the maximum output image size is 1600 × 1200 px.

The nominal linewidth of the laser is 0.003 cm^{-1}, the wavelength is 532 nm, and the repetition rate is 30 Hz. Since the maximum capture rate of the CCD at 1600 × 1200 px is only 7.5 Hz, a frequency divider was applied to divide the Q-switch frequency and the camera trigger rate into 30/5(= 6)Hz. A Stanford DG-645 digital delay system was applied to synchronize the laser pulse and the CCD shutter.

The nominal transmitted wavefront error of the etalon was $\lambda/10$, where $\lambda = 633$ nm, and the nominal wedge angle was less than 1 arc sec. The etalon was mounted on a rotatable mount, so it could be rotated to set the wedge angle on a horizontal plane. The etalon was made by fused silica with the refractive index of 1.461, and was covered with high reflection coatings of 99.5% at 532 nm.

The lens system of the CCD camera was a 150 mm fixed-focal lens (Pentax Takumar 1:4/150), and its focal ratio could be set from $F/22$ to $F/4$. Using a common lens adapter, the focal distance could adjust between 5.5 m to ∞, but a negative focal distance was essential in this experiment since the image distance can be shorter than the focal length. Therefore, a shorter lens adapter was specially designed to reach this negative object distance. The whole camera system was set on a manual translation stage that could move precisely up to 0.01 mm along the x direction.

B. Measuring the Wedge Angle of the Etalon

The wedge angle dh/dx (in radians) needed to be measured before applying Eq. (8) to calculate the image distance.

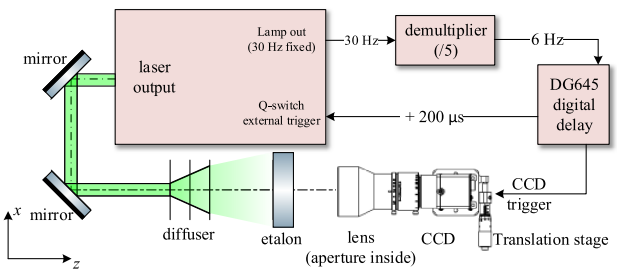

Fig. 3. Experimental configuration.

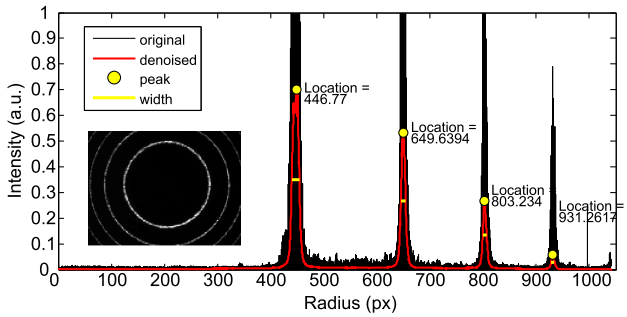

Fig. 4. Interfered spectrum obtained by using the data-folding method and the low-pass filtering method of Huang *et al.*, 2012 [18]. The CCD location was at $x = 0$, and the aperture number was $F/22$.

Since the transmitted wavefront error is less than $\lambda/10$, the conventional equal-thickness interference could hardly measure the wedge angle precisely. The measuring method we chose was to move the CCD system horizontally along the x axis to capture the fringes with different h, and use Eq. (4) to calculate h and dh/dx. The step length of the CCD movement was 0.5 mm, and the aperture number was set as $F/22$.

The method to calculate thickness h from the fringe patterns is demonstrated as below. Figure 4 shows a CCD image captured at the center of the etalon ($x = 0$), and the corresponding spectrum calculated from the image. The data processing algorithm to achieve such a spectrum included the determination of the center, data folding, and low-pass denoising [18]. As shown, the smallest fringe was located at $r = 446.77$ px, so the angle of refraction would be $\theta' = r/f = 446.77 \times 4.4\,\mu m/150$ mm. On the other hand, the order of interference k could be calculated by setting $\theta' = 0$ and using a floor function, as

$$k = \lfloor 2nh_0/\lambda \rfloor = 21954,$$

where h_0 could be set as 4.00 mm exactly, because a small error of k had little effect on the calculation of dh/dx. Applying Eq. (4), the thickness at the center of the etalon was

$$h = (2k\pi)\lambda/\left(4\pi n\sqrt{1 - n^{-2}\theta'^2}\right) = 4 \text{ mm} - 0.4972 \text{ nm}.$$

Using the same method, a series of CCD images were captured as different x locations, and the responding etalon thickness h was calculated. The data curve of $h \sim x$ is shown in Fig. 5(a),

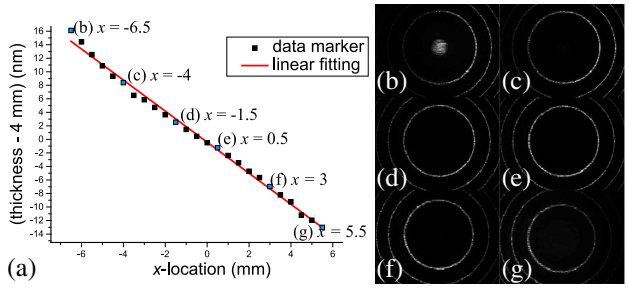

Fig. 5. (a) Linear fitting of the etalon thickness h as a function of CCD location x. Each data marker was calculated from one CCD image. Images of the six blue markers are shown as (b)–(g); noting that a $k + 1$th order of fringe appeared at the center of subfigure (b).

where each marker on the data curve was calculated from one CCD image. The method of least squares was applied to do linear fitting, and the fitting result was

$$\mathrm{d}h/\mathrm{d}x = -2.296\ \mathrm{nm/mm}\ r^2 = 0.9950, \tag{12}$$

where $\mathrm{d}h/\mathrm{d}x$ is the slope of h as a linear function of x and r^2 is the coefficient of determination. As the size of the etalon is $\phi 25.4$ mm, the transmitted wavefront error could be estimated as $25.4\ \mathrm{mm} \times 2.296\ \mathrm{nm/mm} \times (1.461 - 1) = 26.9\ \mathrm{nm} \approx 0.0424\lambda$, and the wedge angle is approximately 0.472 sec arc. These values agreed with the nominal wavefront error ($\leq\lambda/10$) and the nominal wedge angle ($\leq$1 arc sec).

The CCD images shown in Figs. 5(b)–5(g) were captured at $x = -6.5, -4, -1.5, 0.5, 3, 5.5$(mm), respectively. It is obvious to note that the radius of the fringes decreased with x value, and the $(k+1)$th fringe showed a little part at the center of the first image. Another interesting phenomenon is about the brightness of the fringes. Figures 5(d) and 5(e), which were captured near the center of the etalon, showed a uniform brightness distribution; Figs. 5(b) and 5(c), which were captured at the negative side of the x axis, showed a bright right part and a dark left part; while Figs. 5(f) and 5(g), captured at the positive side of the x axis, showed a bright left part and a dark right part. This asymmetric fringe pattern made it difficult to determine the fringe center location precisely. This problem would be very serious if the image was captured far from the etalon center, and that was why Fig. 5(a) only contained data points between $x = -6$ and $x = 6$.

C. Obtaining a High-Resolution Spectrum

The wedge angle $\mathrm{d}h/\mathrm{d}x$ has been measured, so the adjusted image distance could be derived and high-resolution CCD images could be captured. Using Eqs. (12) and (8), the adjusted image distance when $k = 21954$ could be calculated as

$$v = f\left(1 \pm f \cdot \frac{\mathrm{d}h}{\mathrm{d}x} \cdot \frac{k^2\lambda^2}{4h_0^3\sqrt{n^2 - \frac{k^2\lambda^2}{4h_0^2}}}\right)^{-1} = 147.9$$

or 152.1 mm.

In practice, it was difficult to directly measure the image distance, because the precise location of the optical center of the lens was unknown. The focal scale on the lens also did not help on estimating the image distance, because the specially designed lens adapter made the focus scale inaccurate. However, a difference Δz between two different image distances could be measured precisely, by measuring the location of the lens front edge twice. Therefore, if there were an image distance to be measured and a standard image distance f, then the image distance to be measured could be expressed as $f + \Delta z$. The standard image distance was selected to be the focal length f, because it was easy to calibrate by imaging an object very far away.

To test the above calculation of the image distance, three images were captured at image distances of $f - 2.1$ mm, f and $f + 2.1$ mm, respectively, as Figs. 6(a)–6(c) show. The corresponding computer simulations of those three CCD images are shown in Figs. 6(d)–6(f). The aperture number was $F/11$, and the image distances were 147.9, 150, and 152.1 mm, respectively. The experimental results showed very good agreement with the simulations. In comparison with the uniform broadening in Fig. 6(b), the fringe patterns in the left part of Fig. 6(a) and the right part of Fig. 6(c) were obviously narrowed. But considering the negative slope of the etalon, if $v = f - 2.1$ mm, the right part of the fringe—rather than the left part—would be focused, as shown in Fig. 1(b). This confusing fact could be explained by the image inverting process inside the CCD software, because convex lenses produce inverted images. Another interesting fact was that the different fringes broadened to different degrees. For example, the left part of the smallest fringe in Fig. 6(a) was narrowed more than the outside ones. This experimental fact supports the previous conclusion that only one fringe can be accurately focused on the image plane.

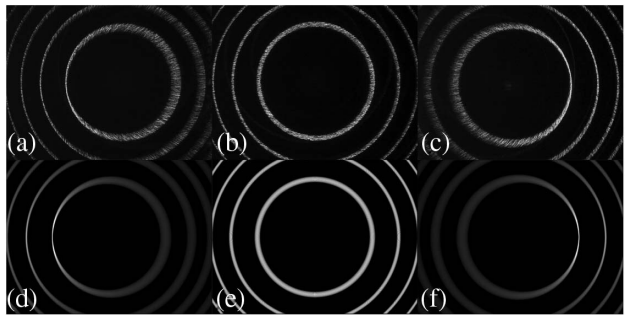

Fig. 6. (a)–(c) Images captured by the CCD camera. The aperture number was $F/11$, and the image distances were $f - 2.1$ mm, f and $f + 2.1$ mm, respectively. (d)–(f) The corresponding simulations. The aperture number was also set as $F/11$, and the image distances were set as 147.9 mm, 150.0 mm, and 152.1 mm, respectively. The sample points array was 15 × 15. The brightness of all these images was increased for a clear display.

Having obtained the focused fringe, the next task would be processing these images and determining the center of the fringes. This step is crucial for the whole processing method, as the precision of the center location would directly affect the precision of the radius. However, because of the asymmetric fringe broadening, the algorithm of Huang *et al.* to determine the centers of the fringes could not be directly applied [18]. A modified algorithm made up of three steps was developed for solving this trouble. The first step was to binarize, erode, and dilate the CCD image, shown in Figs. 7(a)–7(c). Erosion could

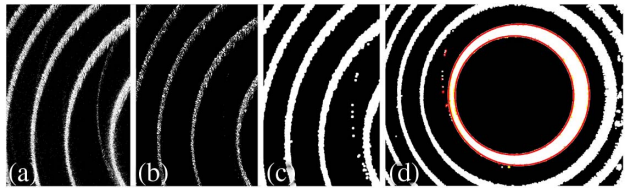

Fig. 7. Processing algorithm to determine the center location of the fringe. (a) Binarization of the original CCD gray-scale image, with a ghost pattern between the first and the second fringe. (b) Erosion of (a), noting that the ghost pattern nearly disappeared. (c) Dilation of (b), noting that the edges became clear. (d) Recognition of edges and the calculation of geometric centers and radii. Using the results, two red circles were drawn on the image, showing a good coincidence with the edges.

erase the ghost patterns on the image, and dilation could make the edges of a fringe clear. The second step was to recognize the inner edge and the outer edge of the fringe and calculate their centers and radii, using the method of Huang *et al.*, as shown in Fig. 7(d). The third step was to calculate the average location of the two centers, and the average location would be used as the center location of the whole fringe.

After determining the center of the fringe, the spectra data could be obtained by data folding and denoising, which were also described by Huang *et al.* [18]. Since the images captured in this experiment were partly focused, the focused part of the image, rather than the whole image, would be folded. For the left-focused fringe [Fig. 6(a)], only pixels inside a central angle $\varphi = 2/7$ rad would be folded. The angle was set toward the left, and its center was set at the center of the fringe. For the right-focused fringe [Fig. 6(c)], the angle was also set to restrict the data-folding range, with its direction toward the right. For the normal-focused fringe [Fig. 6(b)], all the pixels would be folded, just as Huang *et al.* did. These data-folding areas and the corresponding denoised spectra were all shown in Figs. 8(a)–8(c). The horizontal axes of the spectra were transformed from the radius (px) to phase differences using Eq. (4). This transformation could make the peaks uniformly distributed on the horizontal axis. The peaks were marked by Roman numerals, and their corresponding data areas were also marked by the same numeral, as shown in Fig. 8.

To evaluate the resolutions of these three spectra, the FWHM of all the peaks were calculated and marked on Fig. 8. Since only peak I ($k \sim 21954$) was strictly focused on the CCD plane, the FWHM of peak I was used to calculate the finesse and the resolution. As shown in Fig. 8, the FWHM of the left-focused (or right-focused, hereinafter both are referred to as "partly focused") peak I was 0.02 and the FWHM of the normal peak I was 0.12. So it could be concluded that in this experiment, the present method effectively reduced the fringe broadening. The complete data about the finesse and resolution (using Rayleigh criteria) were listed in Table 1.

Table 1. Finesses and Resolutions Calculated from the Three CCD Images

	FWHM		Resolution	
	$(\Delta\delta/2\pi)$	Finesse	(GHz)	(cm^{-1})
Left-focused	0.02	50	0.51	0.017
Normal	0.12	8.3	3.1	0.10
Right-focused	0.02	50	0.51	0.017

D. Discussions

Using the results in Table 1, the hypotheses made in Section 2.A could be checked. The linewidth of the laser was $\Delta\tilde{\nu}_{\text{Laser}} = 0.003\ \text{cm}^{-1}$, while the width of the normal spectrum was $\Delta\tilde{\nu}_{\text{Expri}} = 0.10\ \text{cm}^{-1} \gg \Delta\tilde{\nu}_{\text{Laser}}$. Therefore, the broadening caused by the non-monochromaticity of the laser could be neglected, and hypothesis (a) was valid in this experiment. On the other hand, the FWHM caused by transmitting function Eq. (1) was $\Delta\delta_{\text{Refl}} = 2(1-R)/\sqrt{R} = 0.0100$, where $R = 0.995$, while the width of the normally focused image was $\Delta\delta_{\text{Expri}} = 0.12 \times 2\pi = 0.75 \gg \Delta\delta_{\text{Refl}}$. Therefore, the broadening caused by $R < 100\%$ could be neglected, so hypothesis (b) was also valid. Finally, consider hypothesis (c). Although the

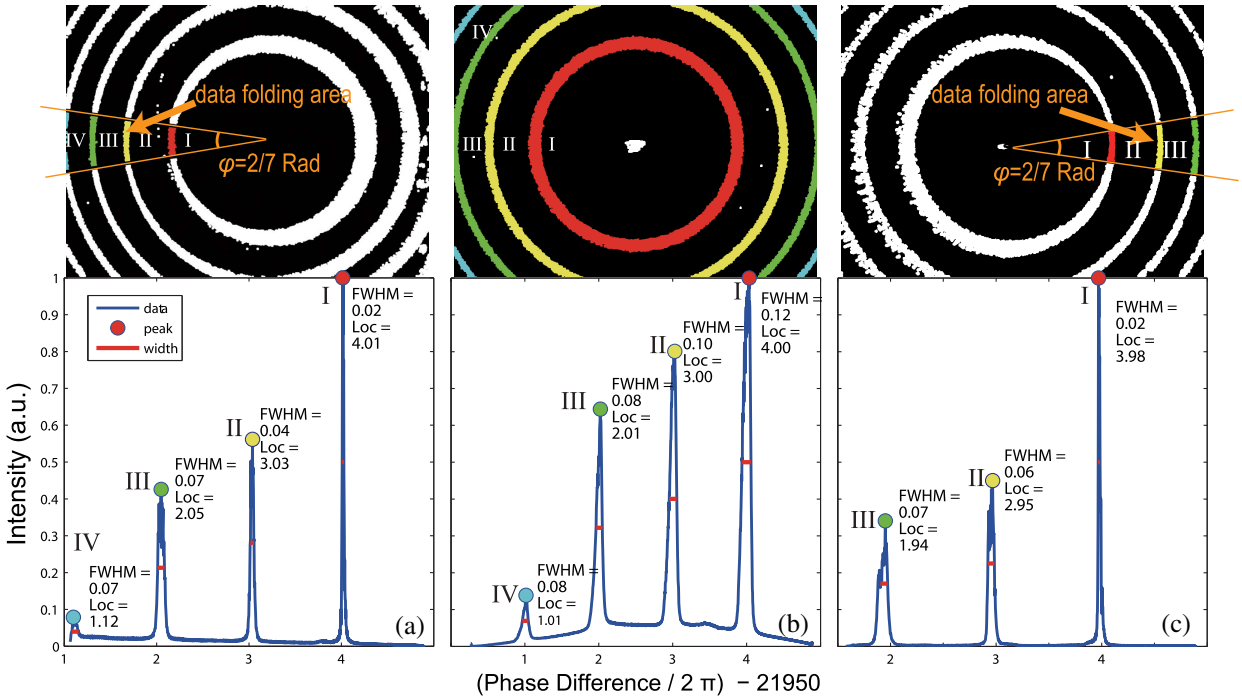

Fig. 8. (a) Spectrum of a left-focused fringe pattern. (b) Spectrum of a normal fringe pattern. (c) Spectrum of a right-focused fringe pattern. The binarized CCD images above the spectra marked the data-folding area using an orange boundary line, and marked the corresponding data area of each peak using Roman numerals and colors.

broadening caused by non-parallelism was effectively reduced, the residual linewidth of the partly focused spectrum was still larger than $\Delta\tilde{\nu}_{\text{Laser}}$ and $\Delta\delta_{\text{Refl}}$. This could be due partly to the fact that the broadening caused by non-parallelism was not perfectly eliminated inside the whole data-folding area, but a more important cause may be that there were other surface defects except non-parallelism. Since the linewidth of the partly focused spectrum was much less than the linewidth of the normal spectrum, the surface defects except non-parallelism could be neglected, and hypothesis (c) was also valid. In conclusion, the fringe broadening of the normal spectrum in this experiment was mostly caused by non-parallelism, and all three hypotheses were valid in this experiment.

The theoretical broadening function of a non-parallel etalon has been derived by previous researchers; therefore, a comparison could be made between the previous work and the data in Table 1. The normalized broadening function derived by Gupta and Prasad [16] was

$$I(\lambda) = \sqrt{1 - [(\lambda - \lambda_0)/D]^2},$$

where $D = \lambda^2/(2K_p nh) \approx \lambda_0^2/(2K_p nh)$, and the non-parallelism was expressed as λ_0/K_p. It should be noticed that the non-parallelism λ_0/K_p was different from the transmitted wavefront error. The non-parallelism was $n\Delta h$, while the transmitted wavefront error was $(n-1)\Delta h$, as the refractive index of air should be considered. The FWHM of this distribution can be derived by setting $I(\lambda) = 1/2$, then λ would be $\lambda = \lambda_0 \pm \sqrt{3}D/2$. So the linewidth was

$$\Delta\lambda = \sqrt{3}D,$$

and

$$\Delta\tilde{\nu} = \frac{\Delta\lambda}{\lambda_0} \times \tilde{\nu}_0 = \frac{\Delta\lambda}{\lambda_0^2} = \frac{\sqrt{3}D}{\lambda_0^2} = \frac{\sqrt{3}}{2K_p nh}. \quad \textbf{(13)}$$

Considering the aperture number $F/11$, K_p could be calculated as $K_p = \lambda/[(f/11)(\mathrm{d}h/\mathrm{d}x)n] = 11.64$, and $\Delta\tilde{\nu}$ could be calculated as $\Delta\tilde{\nu} = \sqrt{3}/(2K_p nh) = 0.1273\ \text{cm}^{-1}$. In comparison with this theoretical prediction, the experimental result was $\Delta\tilde{\nu} = 0.10\ \text{cm}^{-1}$, a little narrower than the prediction. This difference might be attributed to the threshold of the CCD response. There was another evidence which indicated the threshold of the CCD response. This evidence was that the peaks in the normal spectrum [Fig. 8(b)] had different widths, rather than the same width as the theoretical prediction. When there was a threshold on the CCD response curve, the peak would become narrower if the illuminance decreased.

Equation (13) could also be used to estimate the design requirement of the etalon with a given $\Delta\tilde{\nu}$. If another 4-mm etalon was designed to reach a resolution of $0.017\ \text{cm}^{-1}$ (the resolution of the partly focused spectra, shown in Table 1) at $f = 150$ mm and $F/11$, K_p would be $K_p = \sqrt{3}/(2\Delta\tilde{\nu}nh) = 87$. The corresponding transmitted wavefront error would be $(532\ \text{nm}/87)/1.461 \times 25.4\ \text{mm}/(150\ \text{mm}/11) \times (1.461-1) = 3.6\ \text{nm} \approx \lambda/176$, where $\lambda = 632.8$ nm. That means that the transmitted wavefront error of an etalon should be about $\lambda/176$, if it was designed to reach the same resolution as the partly focused fringe pattern. Obviously, reducing the wavefront error to $\lambda/176$ would be time consuming and expensive, while partly focusing could reach the same goal conveniently and economically.

Another method to reduce the broadening is to reduce the aperture. Knowing (f/F number) $\propto \lambda/K_p$ and Eq. (13): $\Delta\tilde{\nu} = \frac{\sqrt{3}}{2K_p nh}$, it could be concluded that

$$\Delta\tilde{\nu} \propto 1/(F\ \text{number}). \quad \textbf{(14)}$$

Using this equation, if $\Delta\tilde{\nu}$ needs to be improved from 3.1 GHz to 0.51 GHz, the aperture should be reduced from $F/11$ to $F/67$. Therefore, the total illuminance on the CCD will drop to $(11/67)^2 \approx 0.026$ of the original value. Using the partly focused method, only pixels inside $\varphi = 2/7$ Rad were folded; therefore, the total effective illuminance will drop to $(2/7)/2\pi \approx 0.046$ of the original value.

In comparison with total luminance, the signal-to-noise ratio (S/N) is a better criterion to evaluate the ability to collect weak signals. The noise on the CCD mainly includes readout noise, thermal noise, and photons from the environment. Since these kinds of noise are nearly the same on every CCD pixel, we can compare the S/N of peak I. Using the partly focused technique, the total noise and total signal will drop to $[(2/7)/2\pi]$ of the original value, and the linewidth of peak I was reduced from 3.1 GHz to 0.51 GHz. Therefore, the $(S/N)'$ of peak I can be calculated as

$$(S/N)' = \frac{[(2/7)/2\pi]S \times (3.1/0.51)}{[(2/7)/2\pi]N} = 6.1(S/N), \quad \textbf{(15)}$$

in which S and N are the total signal and noise of a normal-focused image, respectively. On the other hand, if the aperture was limited from $F/11$ to $F/67$, the total signal will drop $(11/67)^2$, while the total noise will not change. Also considering the linewidth improvement, the $(S/N)''$ of peak I can be calculated as

$$(S/N)'' = \frac{(11/67)^2 S \times (3.1/0.51)}{N} = 0.16(S/N). \quad \textbf{(16)}$$

Comparing $(S/N)'$ and $(S/N)''$, it can be concluded that the signal-to-noise ratio of a partly focused image is much larger than limiting the aperture.

E. Demo Application on Sulfur Hexafluoride

In this subsection, a partly focusing etalon spectrum was used to measure the Brillouin frequency shift of sulfur hexafluoride, a commonly used Brillouin medium in pulse compression [19].

SF_6 gas was compressed in a medium cell up to 2.1 MPa, and the pumping laser was focused into the cell using a $f =$ 100 mm lens. The backward stimulated Brillouin scattering (SBS) beam was split using a $1/4 - \lambda$ wave plate and a polarizing beam splitter, then passed through the diffuser and the etalon, and was captured by the camera. A quartz plate was inserted to reflect a small amount of pumping laser into the etalon as a reference frequency. The whole configuration is shown in Fig. 9. The aperture number was set as $F/11$, while other parameters were the same as the previous experiment. The trigger system was also the same as the previous experiment.

Typical results are shown in Fig. 10. As shown, the pumping frequency and the SBS frequency can be hardly resolved in a normal fringe pattern, since the broadening caused by

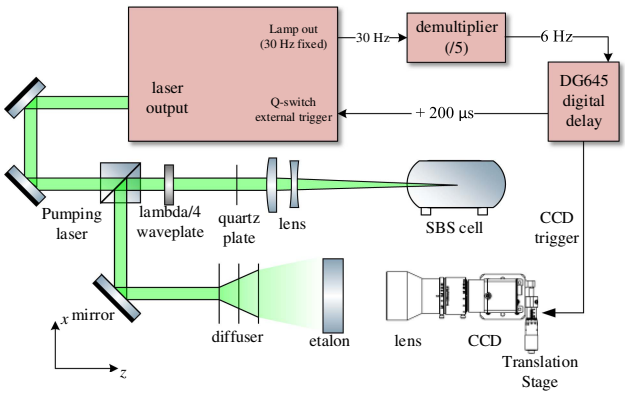

Fig. 9. Experimental setup to measure the Brillouin shift of SF_6.

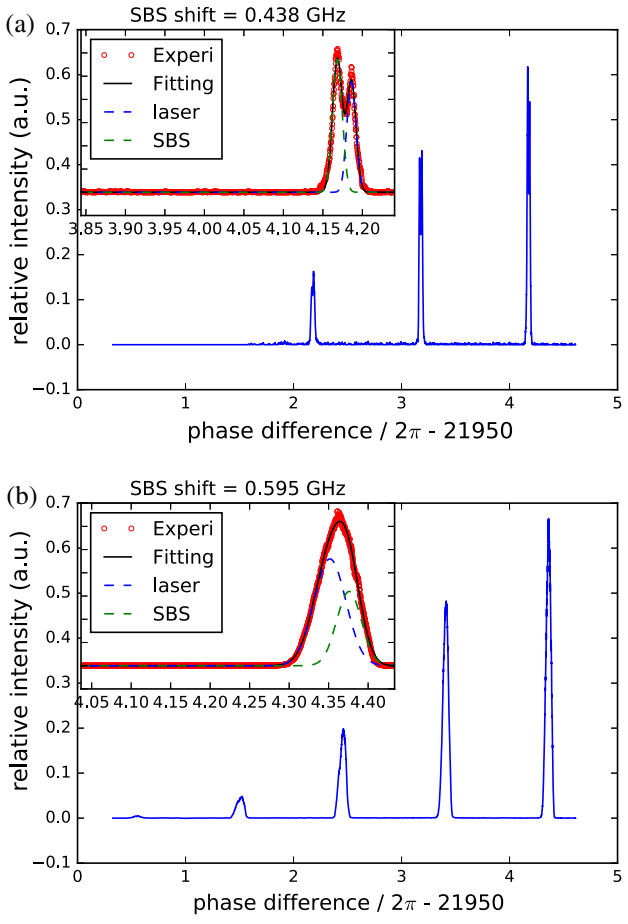

Fig. 10. Typical SBS spectra of SF_6. (a) was from a right-focused fringe pattern, while (b) was from a normal pattern. The inner plots show the details of the highest peak ($k \approx 21954$). Laser peaks and Brillouin peaks were resolved from the double-Gaussian fitting results.

non-parallelism. However, in a right-focused fringe pattern, these two frequencies can be easily resolved. The non-linear least-square method was used to fit the data curve, and the fitting result is $\Delta\nu = 0.438$ GHz. Knowing the wavelength $\lambda = 532$ nm and the refractive index $n = 1.02$ [20], acoustic speed of sulfur hexafluoride can be calculated as $v = \frac{\Delta\nu\lambda}{2n} = 114$ m/s.

The CCD camera had captured 200 images of sulfur hexafluoride, and the mean result is

$$v = 118 \pm 2 \text{ m/s}. \tag{17}$$

This value shows good agreement with the previous result of 113 ± 6 m/s [21].

4. CONCLUSION

In this study, a new method that can improve the resolution of a non-parallel etalon was developed. The method could reduce the fringe broadening caused by non-parallelism. The complete study contained three main points. The first point was deriving a theory to calculate the broadening of a non-parallel etalon at different image distances. Then the wedge angle of the etalon was precisely measured, and the adjusted image distances were calculated. Finally, CCD images were captured at the adjusted image distances, and the captured images were processed to obtain the spectrum. The images and the computer simulation show good agreement, and the resolution of this etalon was effectively improved. In discussions, it was argued that in comparison with improving the etalon or limiting the aperture, this method is more effective, convenient, and economical. An application example was also demonstrated to show the improvement of the etalon resolution.

This method should be useful for most solid etalons, because non-parallelism is the first-order surface error, which is usually larger than other surface defects. However, for some etalons, the main error of which is a second- or higher-order error, this processing method may have a very limited effect. Therefore, future studies should be focused on reducing the broadening caused by high-order surface defects.

Funding. National Natural Science Foundation of China (NSFC) (11475177, 61505210); Innovation Foundation of the Key Laboratory of Chemical Lasers (KLCL-2017-N13).

REFERENCES

1. A. Roche, J. Kumer, R. Nightingale, J. Mergenthaler, G. Ely, P. Bailey, S. Massie, J. Gille, D. Edwards, M. Gunson, M. Abrams, G. Toon, C. Webster, W. Traub, K. Jucks, D. Johnson, D. Murcray, F. Murcray, A. Goldman, and E. Zipf, "Validation of CH_4 and N_2O measurements by the cryogenic limb array etalon spectrometer instrument on the upper atmosphere research satellite," J. Geophys. Res. **101**, 9679–9710 (1996).
2. V. Vassiliev, V. Velichansky, V. Ilchenko, M. Gorodetsky, L. Hollberg, and A. Yarovitsky, "Narrow-line-width diode laser with a high-*Q* microsphere resonator," Opt. Commun. **158**, 305–312 (1998).
3. Q. Wu, R. Gablehouse, S. Solomon, T. Killeen, and C.-Y. She, "A new Fabry–Perot interferometer for upper atmosphere research," Proc. SPIE **5660**, 218–227 (2004).
4. J. Shi, M. Ouyang, W. Gong, S. Li, and D. Liu, "A Brillouin lidar system using F-P etalon and ICCD for remote sensing of the ocean," Appl. Phys. B **90**, 569–571 (2008).
5. X. Ren, Z. Tian, Y. Zhang, L. Wang, and S. Fu, "Theoretical and experimental investigations on measuring underwater temperature by the coherent Brillouin scattering method," Appl. Opt. **54**, 9025–9029 (2015).
6. J. Xu, X. Ren, W. Gong, R. Dai, and D. Liu, "Measurement of the bulk viscosity of liquid by Brillouin scattering," Appl. Opt. **42**, 6704–6709 (2003).

7. D. Liu, J. Xu, R. Li, R. Dai, and W. Gong, "Measurements of sound speed in the water by Brillouin scattering using pulsed Nd:YAG laser," Opt. Commun. **203**, 335–340 (2002).
8. X. He, H. Wei, J. Shi, J. Liu, S. Li, W. Chen, and X. Mo, "Experimental measurement of bulk viscosity of water based on stimulated Brillouin scattering," Opt. Commun. **285**, 4120–4124 (2012).
9. K. Liang, Y. Ma, J. Huang, H. Li, and Y. Yu, "Precise measurement of Brillouin scattering spectrum in the ocean using F-P etalon and ICCD," Appl. Phys. B **105**, 421–425 (2011).
10. E. S. Fry, Y. Emery, X. Quan, and J. W. Katz, "Accuracy limitations on Brillouin lidar measurements of temperature and sound speed in the ocean," Appl. Opt. **36**, 6887–6894 (1997).
11. M. Born and E. Wolf, *Principle of Optics–Electromagnetic Theory and Propagation* (Cambridge University, 1999).
12. R. Hill, "Some fringe-broadening defects in a Fabry–Perot étalon," J. Mod. Opt. **10**, 141–152 (1963).
13. G. Sloggett, "Fringe broadening in Fabry–Perot interferometers," Appl. Opt. **23**, 2427–2432 (1984).
14. J. Ramsay, "Aberrations of Fabry–Perot interferometers when used as filters," Appl. Opt. **8**, 569–574 (1969).
15. E. Palik, H. Boukari, and R. W. Gammon, "Experimental study of the effect of surface defects on the finesse and contrast of a Fabry–Perot interferometer," Appl. Opt. **35**, 38–50 (1996).
16. R. Gupta and C. D. Prasad, "Instrumental broadening caused by the misalignment function in a Fabry–Perot etalon assembly," Appl. Opt. **30**, 373–375 (1991).
17. C. F. McMillan, "Fabry–Perot misalignment: the effect on peak position," Appl. Opt. **25**, 2785–2789 (1986).
18. J. Huang, Y. Ma, B. Zhou, H. Li, Y. Yu, and K. Liang, "Processing method of spectral measurement using F-P etalon and ICCD," Opt. Express **20**, 18568–18578 (2012).
19. R. Fedosejevs and A. Offenberger, "Subnanosecond pulses from a KrF laser pumped SF_6 Brillouin amplifier," IEEE J. Quantum Electron. **21**, 1558–1562 (1985).
20. M. E. Thomas and T. J. Tayag, "Refractive index of He, SF_6, and CO_2 at 0.63299 μm as a function of temperature and pressure," Appl. Opt. **27**, 3317–3318 (1988).
21. V. I. Kovalev, V. I. Popovichev, V. V. Ragul'skii, and F. S. Faizullov, "Gain and line width in stimulated Brillouin scattering in gases," Sov. J. Quantum Electron. **2**, 69–71 (1972).